New fast integrated mobility spectrometer for real-time measurement of aerosol size distribution—I: Concept and theory ☆

Pramod Kulkarni, Jian Wang*

Brookhaven National Laboratory, Building 815E, Upton, NY 11973-5000, USA

Abstract

A new instrument capable of measuring aerosol size distribution with high time and size resolution, and high signal-to-noise ratio is described. The instrument, referred to as *F*ast *I*ntegrated *M*obility *S*pectrometer (FIMS), separates charged particles based on their electrical mobility into different trajectories in a uniform electric field. The particles are then grown into super-micrometer droplets, and their locations on the trajectories are recorded by a fast charge-coupled device (CCD) imaging system. Images captured by the CCD reveal mobility-dependent particle positions and their numbers, which are then used to derive a particle size distribution spectrum. By eliminating the need to scan over a range of voltages, FIMS significantly improves the measurement speed and counting statistics. A theoretical framework has been developed to quantify the measurement range, mobility resolution, and transfer function of FIMS. It is shown that FIMS is capable of measuring aerosol size distributions with high-time and size resolution.
© 2006 Elsevier Ltd. All rights reserved.

Keywords: Aerosol size distribution measurements; High-time resolution; Electric mobility; Transfer function; Particle diffusion; Mobility resolution

1. Introduction

Real-time measurement of particle size distributions, especially in the nanometer size range, is important in many applications such as measurement of atmospheric aerosols and characterization of particles in combustion systems. To capture transient aerosol dynamics occurring on very small time scales, such as in high-temperature environments or other nucleation-dominated systems, fast measurements are often necessary. In other types of measurements, such as aircraft-based studies aimed at characterizing spatial and temporal distributions of atmospheric aerosols, high-time resolution is required to capture variations of aerosol properties over a small spatial domain.

Sub-micrometer aerosol size distributions are mostly measured using electrical mobility techniques, especially for particles with diameter less than 100 nm. There have been considerable advances in electrical mobility-based

* Corresponding author. Tel.: +1 631 344 7920; fax: +1 631 344 2887.

E-mail address: jian@bnl.gov (J. Wang).

measurements, from its early time-intensive days to the current state-of-the-art scanning mobility techniques that take only a few minutes to characterize an entire size distribution spectrum (Flagan, 1998). Electrical mobility-based measurement system often consists of two components: a Differential Mobility Analyzer (DMA) that selects particles within a narrow mobility window (Knutson & Whitby, 1975), and a detector that counts the number of particles within the classified window of mobility. In its early days, mobility-based measurements were made by stepping the classifying voltage of the DMA through a sequence of values to reproduce an entire size distribution, and the measurement time was on the order of 10 min or more. Wang and Flagan (1989) introduced the scanning mobility technique in which the classifying voltage of DMA is continuously scanned. As a result, the time required to measure aerosol size distribution could be substantially reduced to about 1 min. Systems using the scanning mobility technique are often referred to as Scanning Mobility Particle Sizers (SMPS).

There are two obstacles for further accelerating the SMPS measurements. First, faster measurements often result in severely distorted size distributions, which are attributed to the large smearing effect of traditional condensation particle counters (CPCs) used as detectors (Russell, Flagan, & Seinfeld, 1995). To reduce the smearing effect, the scanning mobility techniques have been augmented with time-sensitive detectors. Wang, McNeill, Collins, and Flagan (2002) developed a fast-response mixing condensation nucleus counter (MCNC). They reduced the measurement time to about 3 s by using the MCNC as a detector in SMPS (Wang et al., 2002). The second obstacle to faster SMPS measurements is the low sampling rate and the associated low counting statistics. SMPS systems are based on a sequential measurement technique. Only particles within a narrow range of mobility, which comprise a small fraction of the total aerosol particles introduced into the instrument, are measured at a given time. Whereas, time-sensitive detectors may allow faster measurements, the low counting statistics often require averaging fast measurements over a longer period of time to obtain statistically significant results. This further effectively offsets the reduction in measurement time gained by using the time-sensitive detectors. Other electrical mobility-based instruments include the Electrical Aerosol Spectrometer (EAS) developed by Mirme et al. (1984), (Mirme, 1994; Tammet, Mirme, & Tamm, 1998, 2002). The EAS uses an array of integrated electrometers that operate in parallel in a DMA-like geometry. Since particles of different mobilities are detected simultaneously, EAS is capable of sub-second measurements of aerosol size distributions. Due to the relatively low sensitivity of the electrometers, application of EAS is limited to aerosols with high number concentrations. This instrument has been commercialized by TSI Inc. as Engine Exhaust Particle Sizer (EEPS), and is primarily used for characterizing high concentration engine exhausts (Johnson, Caldow, Pocher, Mirme, & Kittelson, 2004). Besides low sensitivity, EAS and EEPS also have considerably lower size resolution compared to SMPS.

The other type of instruments that are frequently used to measure sub-micrometer aerosol size distributions are Optical Particle Counters (OPCs). For OPC measurements, particle sizes are derived from the intensity of light scattered by particles. OPC offer fast measurement speed and better counting statistics compared to SMPS. However, the measurement range of OPCs is limited to particles with diameters greater than 100 nm. Also, particle physical properties such as shape, refractive index, and morphology have strong influences on derived particle sizes, and are often unavailable. Even for the ideal case of homogeneous spherical aerosol particles, the uncertainty in refractive index often leads to significant uncertainties in derived size distributions (Hering & McMurry, 1991). Furthermore, the interpretation of OPC data is often complicated by Mie resonances in the intensity of light scattered by spherical particles.

Besides SMPS and OPCs, a nucleation-mode aerosol size spectrometer (N-MASS) has been recently developed for fast size distribution measurements onboard a research aircraft (Brock et al., 2000). N-MASS consists of five condensation particle counters operated in parallel at different supersaturations. While N-MASS offers faster measurement speed and better counting statistics than conventional SMPS, it has a limited size resolution (5 size bins), and the measurements are limited to particle diameters less than ∼ 80 nm.

In this paper, we describe a new instrument to measure submicron aerosol size distribution with high-time and size resolution, and high signal-to-noise ratios. The instrument, referred to as Fast Integrated Mobility Spectrometer (FIMS), separates charged particles based on their electrical mobility. Separated particles are then grown, along their trajectories, into super-micrometer droplets in a supersaturated environment and their locations with respect to the electrodes are subsequently detected by a particle imaging system. The imaging system records mobility-dependent particle positions and their numbers, which are then used to derive particle size distribution spectrum. By eliminating the need to scan over a range of voltages, FIMS significantly improves measurement speed and counting statistics. FIMS can perform size distribution measurements with high accuracy and precision in less than a second. This is at least a factor of 50 improvement in the time resolution over traditional SMPS systems. FIMS has a great advantage

over the traditional SMPS in applications involving transient aerosol dynamics, or where measurements with high-time resolutions are required.

2. Working principle of FIMS

The main geometry of FIMS involves a rectangular conduit formed by two parallel plates as shown in Fig. 1(a) and (b). The geometry can be divided into three major sections arranged sequentially—(i) separator, (ii) condenser, (iii) and a detector. As shown in Fig. 1, particle-free sheath flow saturated with a condensing fluid—taken as *n*-butanol in this work—enters the channel parallel to the electrodes from the entrance to the separator. A much smaller aerosol flow (Q_a) carrying charged aerosol particles is introduced into the separator, through a narrow tangential slit that provides a turbulence-free entry. The separator consists of two parallel plate electrodes that generate a uniform electric field in the flow passage. Under the influence of uniform electrical field, the charged aerosol particles are separated into mobility-dependent trajectories. The classified particles subsequently enter the condenser where they are subject to in situ growth by condensation of *n*-butanol contained in the sheath flow. The body of the condenser is isolated from the separator section using electrical insulation. The supersaturation required for condensational growth of particles is created by cooling the walls of the condenser to 5 °C. No electrical field is applied in the condenser; therefore, once
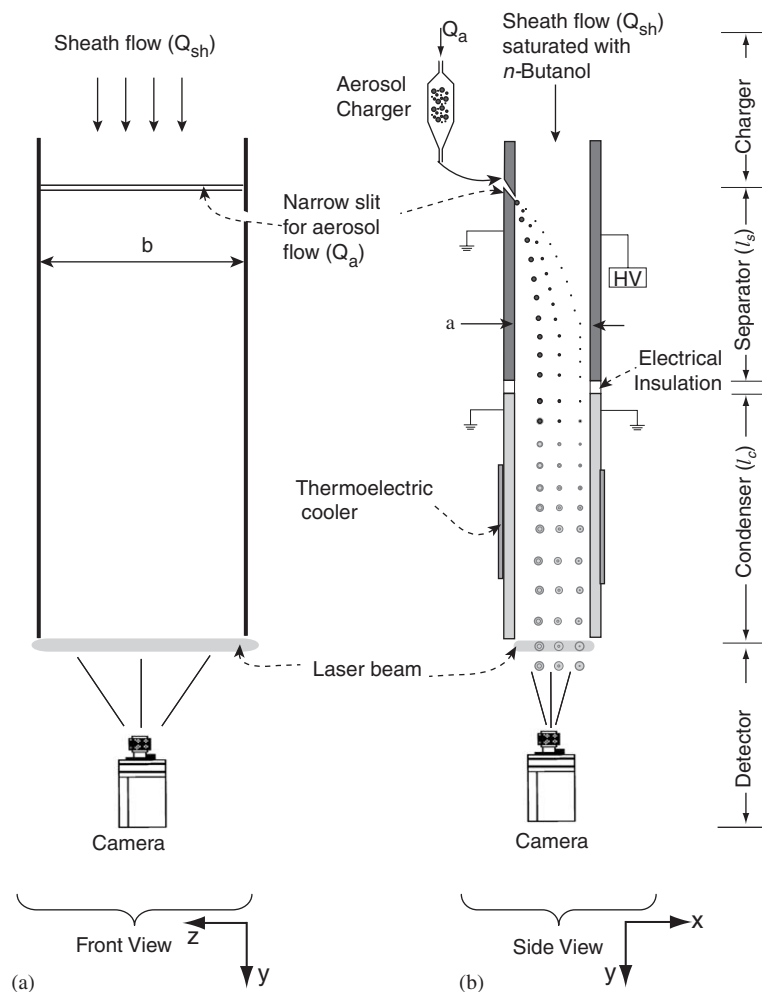

Fig. 1. Schematic figure showing the main components of Fast Integrated Mobility Spectrometer.

the aerosol particles exit the separator, their positions in the direction of the electric field practically remain unaltered. If a proper combination of cooling temperature and residence time is maintained inside the condenser, aerosol particles will grow into super-micrometer droplets by the time they reach the detection zone, which makes their optical detection using a charge-coupled device (CCD) camera feasible.

Since the flow in the channel is a well-developed laminar flow, the displacement of a particle in the direction of the electric field (referred to as x-direction hereafter) is a function of its electrophoretic velocity in the x-direction, and hence a function of its electrical mobility. In other words, the x-coordinate of the particle at the exit of condenser can be directly related to its electrical mobility. A collimated laser beam is used to illuminate the particles as they exit the condenser, and their locations with respect to the two electrodes are subsequently recorded by a high-speed CCD camera. Images recorded by the camera reveal the positions of particles and their numbers, which can be directly used to derive the mobility, and hence aerosol size distribution. As typical CCD cameras can easily acquire images at frame rates of 10 Hz or more, sub-second measurements of particle size distribution are quite feasible using FIMS. By integrating the classification, detection and counting in a single geometry, FIMS eliminates the need for voltage scanning that limits the measurement speed in conventional SMPS.

The electrical mobility of a particle (Z_p) inferred from its x-coordinate in the detection zone depends primarily on the FIMS dimensions, including the distance between the two parallel plates (a), the length of separator (l_s), the voltage (V) applied across the electrodes, the sheath (Q_{sh}) and aerosol flow rate (Q_a). Design of a functional instrument requires knowledge of relationships between these variables. Transfer theory for non-diffusing particles is developed and is discussed below.

3. Transfer theory for non-diffusing particles

The aerosol particles in FIMS are classified based on their electrophoretic drift velocity (v_E) in the uniform electrical field (E_x). This velocity is given by

$$v_E = Z_p E_x, \tag{1}$$

where Z_p is the electrical mobility of the particle:

$$Z_p = \frac{qC_c}{3\pi\mu d_p}, \tag{2}$$

where q is the total electrical charge on the particle, C_c is Cunningham slip correction factor, μ is viscosity of suspending medium, and d_p is the diameter of the particle. The overall transport of particles in the rectangular channel depends on the electrophoretic migration described by above equation, as well as on the aerodynamic flow. In the following analysis, only the central region of the channel cross-section (in x–z plane) is considered, where the flow field is uniform along the z-direction. The flow field in the central region of parallel plate geometry can be described using a two-dimensional stream function $\Psi(x, y)$, which is defined in Cartesian coordinates as

$$\Psi(x, y) \equiv \int^{x, y} [u_y \, dx - u_x \, dy], \tag{3}$$

where u_x and u_y are fluid flow velocities in the x- and y-direction, respectively. Similarly, an electric flux function Φ is defined as

$$\Phi(x, y) \equiv \int^{x, y} [E_y \, dx - E_x \, dy], \tag{4}$$

where E_x and E_y are electrical field strengths in x- and y-direction, respectively. Note that $E_y = 0$ in this study. Analogous to fluid stream function, non-diffusing particles follow trajectories that correspond to constant particle stream functions defined as (Knutson & Whitby, 1975),

$$\Gamma(x, y) \equiv \Psi + Z_p \Phi = \text{constant}. \tag{5}$$

Consider a non-diffusing particle that is introduced into the separator section. It is then required to know the probability of finding a particle at a given location x or flow streamline Ψ at the end of the separator (i.e. at $y = l_s$). As there
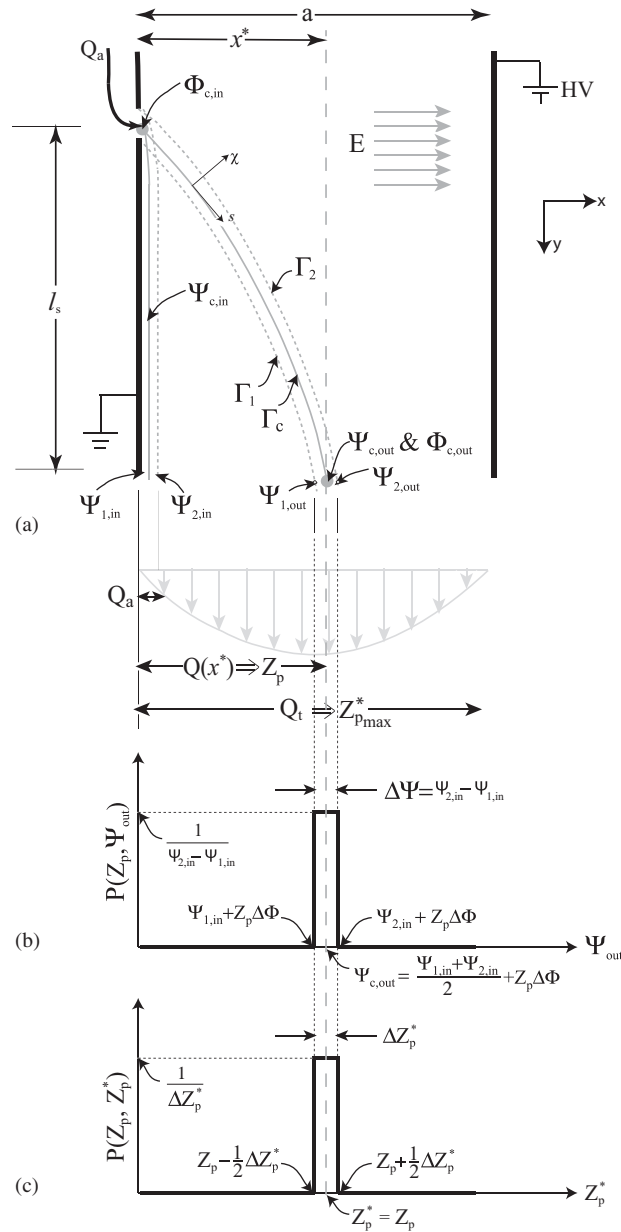
Fig. 2. (a) Definition of key streamlines used in derivation of the FIMS transfer function. Also shown are key features of (b) non-diffusing transfer function in Ψ coordinate space, and (c) in Z_p^* coordinate space.

is no change in the x-coordinate of the particle through the condenser ($E_x = 0$ in condenser), it suffices to consider the probability density at $y = l_s$. For non-diffusing particles an approach similar to that of Stolzenburg's (1988) is used to derive this probability density function, also referred to as the transfer function in this work. The definitions of key streamlines are shown in Fig. 2. Let $\Psi_{1,in}$ and $\Psi_{2,in}$ be the two streamlines that bound the aerosol flow at the inlet. Subscripts in and out denote the location of a streamline at the entrance and exit of separator, respectively. The probability density function $P(Z_p, \Psi_{out})$, which dictates the probability of finding a particle with mobility Z_p that exits between streamlines Ψ_{out} and $(\Psi_{out} + d\Psi_{out})$ is then given by

$$P(Z_p, \Psi_{out}) \, d\Psi_{out} = \left[\int_{\Psi_{1,in}}^{\Psi_{2,in}} f_e(\Psi_{in}) \cdot f_{t-nd}(Z_p, \Psi_{in}, \Psi_{out}) \, d\Psi_{in} \right] d\Psi_{out}, \tag{6}$$

where $f_e(\Psi_{in}) \, d\Psi_{in}$ is the probability that the particle is introduced between streamlines Ψ_{in} and $(\Psi_{in} + d\Psi_{in})$ at the separator entrance, and is given by

$$f_e(\Psi_{in}) = \frac{1}{\Psi_{2,in} - \Psi_{1,in}}. \tag{7}$$

$f_{t-nd}(Z_p, \Psi_{in}, \Psi_{out}) \, d\Psi_{out}$ in Eq. (6) is probability of a non-diffusing particle exiting the separator between streamlines Ψ_{out} and $(\Psi_{out} + d\Psi_{out})$ when it enters the separator at Ψ_{in}. Since the trajectory of a non-diffusing particle corresponds to a constant particle streamline function, this probability can be expressed as (Stolzenburg, 1988)

$$\begin{aligned} f_{t-nd}(Z_p, \Psi_{in}, \Psi_{out}) = \delta(\Gamma_{out} - \Gamma_{in}) &= \delta(\Psi_{out} - \Psi_{in} - Z_p(\Phi_{in} - \Phi_{out})) \\ &= \delta(\Psi_{out} - \Psi_{in} - Z_p \Delta\Phi), \end{aligned} \tag{8}$$

where δ is a delta function, and $\Delta\Phi = \Phi_{in} - \Phi_{out}$. The probability distribution function can be obtained by inserting Eqs. (7) and (8) into Eq. (6) as follows:

$$P(Z_p, \Psi_{out}) = \frac{1}{\Psi_{2,in} - \Psi_{1,in}} \int_{\Psi_{1,in}}^{\Psi_{2,in}} \delta(\Psi_{out} - \Psi_{in} - Z_p \Delta\Phi) \, d\Psi_{in}. \tag{9}$$

After performing the integration, the above equation can be rewritten as

$$P(Z_p, \Psi_{out}) = \frac{1}{2} \frac{1}{\Psi_{2,in} - \Psi_{1,in}} [H(\Psi_{out} - \Psi_{1,in} - Z_p \Delta\Phi) - H(\Psi_{out} - \Psi_{2,in} - Z_p \Delta\Phi)], \tag{10}$$

where $H(x)$ is a modified Heaviside step function defined as, $H(x) \equiv 2 \int_0^x \delta(x') \, dx'$. The value of $H(x)$ is 1 for $x > 0$, 0 for $x = 0$, and -1 for $x < 0$. Eq. (10) gives the probability density of finding a non-diffusing particle with mobility Z_p at Ψ_{out}, and is graphically shown in Fig. 2(b). As it is a subtraction of two Heaviside step functions, the shape of $P(Z_p, \Psi_{out})$ is a rectangle. The value of $P(Z_p, \Psi_{out})$ is $1/(\Psi_{2,in} - \Psi_{1,in})$ when $\Psi_{1,in} + Z_p \Delta\Phi < \Psi_{out} < \Psi_{2,in} + Z_p \Delta\Phi$, and zero elsewhere. Consider trajectories of particles introduced along the centroid flow streamline, $(\Psi_{1,in} + \Psi_{2,in})/2$ at the aerosol inlet; since the particle streamline function remains constant along particle trajectories

$$\Psi_{c,out} + Z_p \Phi_{c,out} = \Psi_{c,in} + Z_p \Phi_{c,in} = \frac{\Psi_{1,in} + \Psi_{2,in}}{2} + Z_p \Phi_{c,in}. \tag{11}$$

From Eq. (11), the particle mobility Z_p is expressed as

$$Z_p = \frac{\Psi_{c,out} - [(\Psi_{1,in} + \Psi_{2,in})/2]}{\Phi_{c,in} - \Phi_{c,out}} = \frac{\Psi_{c,out} - [(\Psi_{1,in} + \Psi_{2,in})/2]}{\Delta\Phi}. \tag{12}$$

In order to facilitate subsequent discussion on measurement resolution and performance of FIMS, a new variable called instrument response mobility Z_p^* is introduced, and is defined as

$$Z_p^* \equiv \frac{\Psi_{out} - [(\Psi_{1,in} + \Psi_{2,in})/2]}{\Delta\Phi}. \tag{13}$$

The instrument response mobility Z_p^* is uniquely related to Ψ_{out} according to the above equation. From this definition it then follows that, when a particle with mobility Z_p is introduced at the inlet, the probability of its mobility being measured between Z_p^* and $(Z_p^* + dZ_p^*)$ is given by $P(Z_p, Z_p^*) \, dZ_p^* = P(Z_p, \Psi_{out}) \, d\Psi_{out}$. The probability density function based on the new variable Z_p^* is given by

$$\begin{aligned} P(Z_p, Z_p^*) &= P(Z_p, \Psi_{out}) \frac{d\Psi_{out}}{dZ_p^*} \\ &= P(Z_p, \Psi_{out}) \Delta\Phi \\ &= \frac{1}{2} \frac{\Delta\Phi}{\Psi_{2,in} - \Psi_{1,in}} [H(\Psi_{out} - \Psi_{1,in} - Z_p \Delta\Phi) - H(\Psi_{out} - \Psi_{2,in} - Z_p \Delta\Phi)]. \end{aligned} \tag{14}$$

$P(Z_p, Z_p^*)$ can be further simplified, by inserting Eq. (13) into Eq. (14), to the following form:

$$
\begin{aligned}
P(Z_p, Z_p^*) &= \frac{1}{2} \frac{\Delta\Phi}{\Psi_{2,in} - \Psi_{1,in}} \left[H\left(Z_p^* \Delta\Phi + \frac{\Psi_{2,in} - \Psi_{1,in}}{2} - Z_p \Delta\Phi \right) \right. \\
&\quad \left. - H\left(Z_p^* \Delta\Phi - \frac{\Psi_{2,in} - \Psi_{1,in}}{2} - Z_p \Delta\Phi \right) \right] \\
&= \frac{1}{2\Delta Z_p^*} \left\{ H\left[\Delta\Phi \left(Z_p^* - Z_p + \frac{1}{2}\Delta Z_p^* \right) \right] - H\left[\Delta\Phi \left(Z_p^* - Z_p - \frac{1}{2}\Delta Z_p^* \right) \right] \right\} \\
&= \frac{1}{2\Delta Z_p^*} \left\{ H\left[Z_p^* - \left(Z_p - \frac{1}{2}\Delta Z_p^* \right) \right] - H\left[Z_p^* - \left(Z_p + \frac{1}{2}\Delta Z_p^* \right) \right] \right\},
\end{aligned}
\tag{15}
$$

where

$$
\Delta Z_p^* = \frac{\Psi_{2,in} - \Psi_{1,in}}{\Delta\Phi}.
$$

Fig. 2(c) graphically depicts the nature of $P(Z_p, Z_p^*)$ for non-diffusing particles. Comparing Eq. (12) and (13), it can then be seen that particles that enter on the centroid streamline (i.e. $\Psi_{c,in}$) at the aerosol inlet will have the instrument response mobility (Z_p^*) the same as their particle mobility (Z_p). $P(Z_p, Z_p^*)$ characterizes the response of the instrument to non-diffusing particles with mobility Z_p, which is a distribution shown in Fig. 2(c). The centroid of this distribution is located at the particle mobility Z_p, and the probability is constant between $(Z_p - \frac{1}{2}\Delta Z_p^*)$ and $(Z_p + \frac{1}{2}\Delta Z_p^*)$. The spread of the probability density function $P(Z_p, Z_p^*)$ (also referred as the transfer function) is an indicator of measurement uncertainty. For non-diffusing particles, the uncertainty is caused by finite width of aerosol flow stream. Particle diffusion contributes to additional uncertainty in mobility measurements, and will be discussed in detail later.

From the definition of the flow streamline function, we have

$$
\Psi_{out} - \Psi_{1,in} = \int_0^x u_y \, dx' = \frac{1}{b} \left[b \cdot \int_0^x u_y \, dx' \right] = \frac{Q(x)}{b},
\tag{16}
$$

where $Q(x)$ is the volumetric flow rate of the flow between the streamlines Ψ_{out} and $\Psi_{1,in}$, and x is the location of Ψ_{out} at the separator exit. Similarly, it can be shown that

$$
\Psi_{2,in} - \Psi_{1,in} = Q_a/b,
\tag{17}
$$

$$
\Delta\Phi = \int_{l_s}^0 -E_x \, dy = E_x l_s.
\tag{18}
$$

The forgoing analysis assumes uniform flow field in z-direction. In other words, only the central region of the separator cross-section (in x–z plane) is considered, and the edge effects from channel walls (in x–y planes) on both sides of the view region are neglected. Correspondingly, all flow rates used in the analysis are based on two-dimensional flow field extending to a full-width (b) of the separator channel (see Fig. 2). The analysis is substantially simplified by using this "effective" flow rate. However, the actual flow rate in the corresponding geometry in FIMS will be slightly lower than this "effective" flow rate due to channel walls in the x–y plane. Instrument response mobility Z_p^* can be obtained, by inserting Eqs. (16), (17) and (18) into Eq. (13), as follows:

$$
Z_p^* = \frac{Q(x) - (Q_a/2)}{b l_s E_x}.
\tag{19}
$$

The flow field in the central region of the separator can be described by a two-dimensional flow between two parallel plates, with a parabolic velocity profile given by (Bird, Stewart, & Lightfoot, 1960)

$$
u_y(\tilde{x}) = \frac{6Q_t}{ab}[\tilde{x}(1 - \tilde{x})], \quad 0 \leqslant \tilde{x} \leqslant 1,
\tag{20}
$$

where $\tilde{x}$ is the normalized x-coordinate defined as $\tilde{x} = x/a$, and Q_t the total flow rate through the separator, and is sum of Q_a and Q_{sh}. $Q(\tilde{x})$ can be expressed as follows by using Eq. (20):

$$Q(\tilde{x}) = ab \int_0^{\tilde{x}} u_y(\tilde{x}')\, d\tilde{x}' = Q_t(3\tilde{x}^2 - 2\tilde{x}^3). \tag{21}$$

Eq. (19) can be used along with Eq. (21) to calculate instrument response mobility Z_p^* for a given $\tilde{x}$.

Eq. (19) shows that maximum mobility, $Z_{p_{max}}^*$, measured by FIMS corresponds to $Q(\tilde{x} = 1) = Q_t$. Let β denote the ratio of aerosol to sheath flow rate (Q_a/Q_{sh}). The the total flow rate can be expressed as $Q_t = Q_a((1 + \beta)/\beta)$. The following equation for response mobility can be obtained by using the definitions of $Z_{p_{max}}^*$ and β, along with Eqs. (19) and (21):

$$\frac{Z_p^*}{Z_{p_{max}}^*} = \frac{2(1 + \beta)(3\tilde{x}^2 - 2\tilde{x}^3) - \beta}{2 + \beta}. \tag{22}$$

For $\beta \ll 1$ ($\beta = 0.02$ for suggested operating conditions), the above equation can be further simplified (within 1% accuracy) to

$$\frac{Z_p^*}{Z_{p_{max}}^*} = (1 + \beta)(3\tilde{x}^2 - 2\tilde{x}^3) - \frac{\beta}{2}. \tag{23}$$

4. Design considerations

4.1. Mobility resolution and instrument measurement range

As discussed earlier, the maximum mobility ($Z_{p_{max}}^*$) that can be measured in a single geometry is obtained when $Q(\tilde{x} = 1) = Q_t$, and is given by

$$Z_{p_{max}}^* = \frac{Q_t - (Q_a/2)}{bl_s E_x} = \frac{Q_a((2 + \beta)/2\beta)}{bl_s E_x} \cong \frac{Q_a}{\beta\,(bl_s E_x)}. \tag{24}$$

Similarly, the minimum mobility ($Z_{p_{min}}^*$) is obtained when $Q(\tilde{x}) = Q_a$, and is given by

$$Z_{p_{min}}^* = \frac{Q_a}{2(bl_s E_x)}, \tag{25}$$

$Z_{p_{min}}^*$ and $Z_{p_{max}}^*$ represent the maximum range of particle mobility that can be measured in a single FIMS unit. Theoretically, for $\beta = 0.02$, range covering a factor of 100 in electrical mobility can be measured in a single FIMS unit. However, the practically useful range can only be obtained by examining the uncertainties associated with the mobility measurements over this range. Assuming the particle position at the separator exit can be measured with sufficiently high accuracy, for a non-diffusing particle the uncertainty in measured mobility can be attributed to the finite stream width of aerosol flow. However this uncertainty, characterized by ΔZ_p^*, can be readily obtained by examining the width of probability density function $P(Z_p, Z_p^*)$ given by Eq. (15). Thus,

$$\Delta Z_p^* = \frac{\Psi_{2,in} - \Psi_{1,in}}{\Delta\Phi} = \frac{Q_a}{bl_s E_x}. \tag{26}$$

Eq. (26) shows that the uncertainty in instrument response mobility is constant regardless of the particle mobility. Comparing Eqs. (24) and (26), ΔZ_p^* can be rewritten as

$$\Delta Z_p^* \cong \beta Z_{pmax}^*. \tag{27}$$

To quantify the relative uncertainty in measured mobility, which is often more important than the absolute uncertainty itself, mobility resolution R is introduced, and is defined as (Flagan, 1999)

$$R = \frac{Z_p}{\Delta Z_{fwhh}^*}, \tag{28}$$

Table 1
(a) Key geometric dimensions of the proposed FIMS units

Dimension	Unit 1	Units 2–4
Distance between electrode plate, a (cm)	1	1
Width of plate electrodes, b (cm)	10	10
Length of plate electrodes, l_s (cm)	5	20
Length of condenser, l_c (cm)	30	30

(b) Operating parameters of the four FIMS units that cover the particle size range from 5 to 1000 nm at $\beta = 0.02$

Unit	$Z_{p_{max}}$	Diameter range (nm)	Voltage (V)		
			$Q_t = 9.7$ lpm $Q_a = 0.19$ lpm	$Q_t = 11.85$ lpm $Q_a = 0.23$ lpm	$Q_t = 15$ lpm $Q_a = 0.3$ lpm
1	8.60×10^{-6}	5–15	37.52	45.84	58.02
2	9.75×10^{-7}	15–47	73	90	128
3	1.07×10^{-7}	47–173	750	916	1202
4	1.07×10^{-8}	173–1000	7411	9054	11461

where, ΔZ_{fwhh}^* is full-width of the probability density function at half its maximum height. For non-diffusing particles, $\Delta Z_{fwhh}^* = \Delta Z_p^*$, and R is given by

$$R = \frac{Z_p}{\Delta Z_p^*} \tag{29}$$

where the definition of ΔZ_p^* is given in Eq. (26). A higher resolution corresponds to lower relative uncertainty in measured particle mobility. An expression for resolution R can be obtained by inserting Eqs. (19) and (26) into Eq. (29) as

$$R = \frac{Z_p}{\Delta Z_p^*} \cong \frac{Z_p}{\beta Z_{p_{max}}^*} = \frac{1}{\beta \tilde{Z}_{p_{max}}^*}, \tag{30}$$

where $\tilde{Z}_{p_{max}}^* = Z_{p_{max}}^*/Z_p$. As ΔZ_p^* is constant, the mobility resolution R increases with increasing Z_p. The resolution reaches its maximum value $R_{max} = 1/\beta$ at the maximum response mobility $Z_{p_{max}}^*$ ($\tilde{Z}_{p_{max}}^* = 1$). At $\beta = 0.02$, $R_{max} \sim 50$. If the minimum acceptable resolution (R_{min}) is set to 5, we have $R_{min} = 0.1 \times R_{max}$, and $Z_{p_{min}}^* = 0.1 \times Z_{p_{max}}^*$. Thus, a decade of mobility can be measured in a single FIMS unit with acceptable resolution. Four FIMS units, operating simultaneously, will be required to measure the entire sub-micrometer size range, from 5 to 1000 nm, with the highest possible time resolution. Based on the above analysis, the key dimensions of four FIMS units have been calculated and are listed in Table 1. It is worth pointing out that, even though the dimensions of the flow channel are 1 cm × 10 cm (in x–z plane) according to Table 1, the actual area of interest is the central 1 cm × 5.6 cm portion of the channel. In other words, only particles detected in this region are used to derive particle size distributions. This is to avoid the edge effects of flow introduced by the channel walls in x–y plane. The physical dimensions are the same for Units 2–4, and the only difference is the voltage applied across the electrodes. As Unit 1 measures particles in the lowest size range, the length of plate electrode is reduced to 5 cm to minimize degradation of resolution of small particles due to Brownian diffusion. The separator voltage for each unit is listed in Table.1 at three different flow rates. It is worth noting that the choice of physical dimensions and operating conditions given here is only one from many possibilities. For instance, the measurement range of a single FIMS can be increased to a factor of 20 in mobility by operating at a higher flow rate ratio $\beta = 0.01$ (with a minimum resolution of 5). If the same total flow rate Q_t is maintained, the reduced aerosol flow rate at $\beta = 0.01$ will lead to lower counting statistics. On the other hand, if the same aerosol flow rate is maintained at $\beta = 0.01$, the total flow rate Q_t will double, and a longer condenser will be required to grow particles into detectable droplets. For different measurement requirements, the physical dimensions and operating conditions can be optimized to achieve the best combination of measurement range, resolution, and counting statistics.

The physical dimensions and the flow rates of the FIMS directly influence the degree of saturation that can be attained in the condenser, which in turn determine whether the particles will grow into optically detectable droplets.

Table 2
Parameters used in particle growth simulations

Parameters	Values/expressions
Saturation vapor pressure of butanol, p_{sat}	$10^{\left(7.4768 + \frac{1362.39}{94.42 + T}\right)}$
Molecular weight of butanol, M_b	$74.123 \, \text{g mole}^{-1}$
Surface tension of butanol, σ_s	$24.6 \, \text{dyn cm}^{-1}$
Effective diffusivity of butanol, D_v	$D_v' = D_v \left/ \left(1 + \left(\frac{2D_v}{\alpha_c d_p}\right)\left(\frac{2\pi M_a}{RT}\right)^{1/2}\right)\right.$
Diffusivity of butanol, D_v	$0.0810 \, \text{cm}^2 \, \text{s}^{-1}$
Density of butanol, ρ_l	$0.810 \, \text{g cm}^{-3}$
Effective thermal diffusivity of air, k_a'	$k_a' = k_a \left/ \left(1 + \left(\frac{2k_a}{\alpha_T d_p \rho c_p}\right)\left(\frac{2\pi M_a}{RT}\right)^{1/2}\right)\right.$
Thermaldiffusivity of air, k_a	$(4.39 + 0.071 \, T) \times 10^{-3}$
Heat capacity of air, c_p	$1.005 \, \text{J g}^{-1} \, \text{K}^{-1}$
Mass and thermal accommodation coefficients, α_c, and α_T	0.045
Latent heat of butanol, ΔH_v	$583 \, \text{J g}^{-1}$

Detailed numerical simulations were carried out to model the performance of the instrument with a focus on degree of supersaturation and growth kinetics of particles in the condenser, and are discussed below.

4.2. Saturation profile in condenser

Simulations were performed to obtain the contour profile of saturation ratios of n-butanol in the condenser using the FIMS dimensions listed in Table 1. Simulations involving discrete particle transport that incorporated their convective and diffusional transport and their condensational growth were also performed to estimate their final droplet sizes in the detection region.

Coupled partial differential equations describing momentum transfer (to obtain flow velocities in x-, and y-direction), mass transfer (spatial distribution of n-butanol), and heat transfer (temperature profile) were first solved using multiphysics computing software (FEMLAB 3.0; Comsol, Inc.) employing finite element methods (FEM). A simplified, 2D parallel-plate geometry representing the main rectangular conduit in x–y plane was considered in the computations (Fig. 1(b)). Sufficiently long entrance region was provided before the separator to allow fully developed laminar flow in the channel. A 2 cm buffer zone (in y-direction) was provided to electrically insulate the separator HV electrode from the condenser. Aerosol flow was introduced through a narrow slit, 1 mm wide, into the separator at an angle of $30°$. The temperature of aerosol and sheath flow entering the channel was assumed at $25°C$. The sheath flow entering the separator was assumed saturated with n-butanol. The walls of the separator were maintained at $30°C$, and that of the condenser were kept at $5°C$. The vapor pressure of butanol (p) at the channel walls was assumed to be in equilibrium with local temperature, i.e. $p = p_{sat}$, and was computed using Antoine equation listed in Table 2. The local saturation ratio was defined as $S = p/p_{sat}$, where p is the local vapor pressure of butanol. The Kelvin equivalent diameters (d_{pKel}) associated with the saturation ratio was also calculated using the following equation:

$$d_{pKel} = \frac{4\sigma_s M_b}{\rho_l RT \, \log \, S},$$
(31)

where R is universal gas constant, and S is saturation ratio. The definitions of remaining terms in the above equation, and their values used in computation are listed in Table 2. To obtain a conservative estimate, calculations for supersaturation ratios were performed at a total flow rate of $Q_t = 15$ lpm.

Fig. 3 shows contour plots of the saturation ratios (black solid lines) and equilibrium Kelvin diameters (gray dotted lines) in the condenser of the FIMS. Saturation ratios are substantially higher than 1 in most of the condenser, and high saturation ratios up to 5 occur in the central region of the condenser. The corresponding equilibrium Kelvin
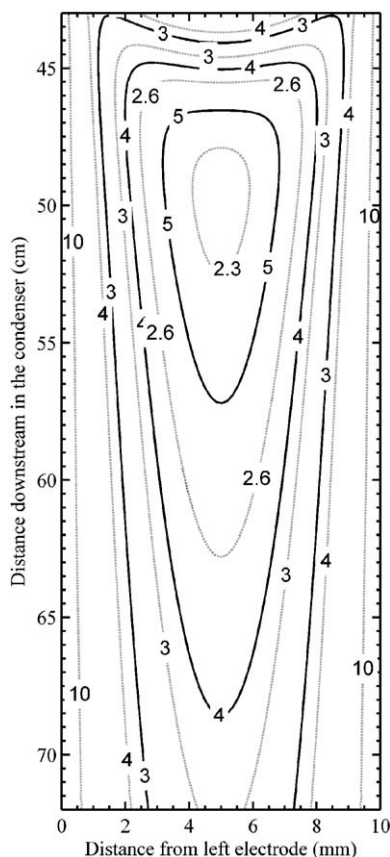
Fig. 3. Contour plot showing simulated distributions of saturation ratios (solid black lines) of *n*-butanol and equilibrium Kelvin diameters (gray dotted line, nm) inside the condenser.

diameter (d_{pKel}), which represents the diameter of the smallest particle that can be activated, is less than 5 nm in almost entire condenser region. In an actual system, the saturation ratios could be slightly lower compared to the values shown in Fig. 3 due to butanol depletion onto particles and non-idealities in temperature control. The butanol concentration of the sheath flow also influences the final saturation ratios attained in the condenser.

4.3. Particle transport and growth simulations

To ensure that particles grow into optically detectable sizes once they are activated, calculations were performed to obtain the final sizes of grown droplets at the end of the condenser. Simulations involving discrete Brownian motion and convective transport of particles were performed using a Brownian dynamics approach. The flow, temperature, and saturation profiles were obtained from FEM simulations described earlier. The motion of the particle was modeled using a modified Langevin equation (Ermak, 1975)

$$\mathbf{r}(t + \Delta t) = \mathbf{r}(t) + \left(\mathbf{v}_f + \frac{D(T, d_p)}{k_B T} \mathbf{F}_{ext}(t) \right) \Delta t + \delta \mathbf{r}_G, \tag{32}$$

where $\mathbf{r}(t+\Delta t)$ is the position vector of particle at time $(t+\Delta t)$, $\mathbf{r}(t)$ is the position vector at time t, $\mathbf{v}_f$ is the deterministic particle velocity vector resulting from fluid flow, $D(T, d_p)$ is the temperature-, and size-dependent diffusion coefficient of particle, $\mathbf{F}_{ext}(t)$ is the total external force vector acting on the particle, k_B is the Boltzmann's constant, and T is the temperature of the surrounding fluid. $\delta \mathbf{r}_G$ in the above equation represents Gaussian random displacement due to particle diffusion and is chosen independently from a Gaussian distribution with a zero mean and variance equal to $\langle (\delta \mathbf{r}_G)^2 \rangle = 2D \delta t$.
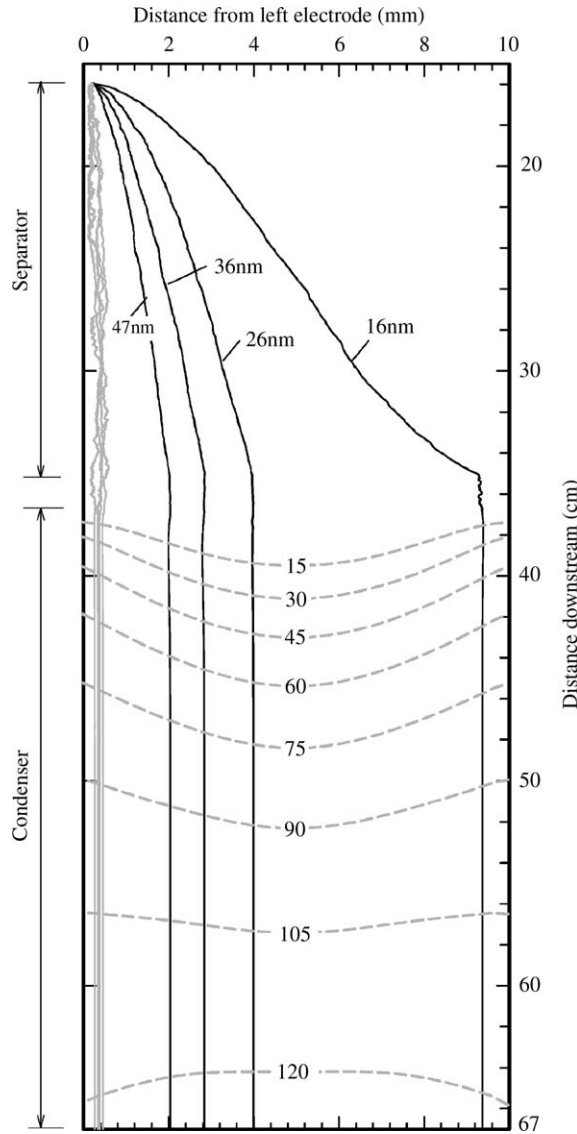
Fig. 4. Trajectories of charged and uncharged particles in FIMS. Also shown are contours representing spatial distribution of grown droplet diameters for 5 nm seed particle.

Simulations involved releasing a particle of given diameter at $x = 0$ with their y-coordinate randomly distributed over the aerosol entrance slit, followed by evolving its trajectory in finite time steps Δt according to Eq. (32). The particle was also subject to condensational growth according to the following growth law (Seinfeld & Pandis, 1998)

$$d_p \frac{dd_p}{dt} = \frac{S - \exp(4M_b \sigma_s / RT \rho_l d_p)}{(\rho_l RT / 4 p_{sat} D'_v M_b) + (\Delta H_v \rho_l / 4 k'_a T)((\Delta H_v M_b / RT) - 1)}. \tag{33}$$

Table 2 lists notations and values of key parameters used in the above equation. Fig. 4 shows trajectories of both charged and uncharged particles with diameters of 16, 26, 36, and 47 nm in Unit 2 at $Q_t = 15$ lpm, and $Q_a = 0.3$ lpm. The Brownian nature of trajectories is clearly visible. Also, note as particles enter the condenser, they quickly grow into larger droplets, resulting in negligible Brownian motion, and changes in their x-coordinate in the condenser. Table 3 compares the x-coordinate of particles at the end of the separator and condenser. The change in x-coordinate is indeed negligible. It is worth noting that these numerical simulations account for changes in flow velocities due to the

Table 3
Summary of particle transport and growth simulations

Diameter, d_p (nm)	x-coordinate of particle (mm)	
	$y^a = l_s$	$y = l_s + l_c$
15	9.619	9.612
18	6.488	6.469
26	3.953	3.948
36	2.795	2.802
47	2.101	2.104

Results are averaged over 10 replicate simulations.
[a]Distance from aerosol entrance.

non-uniform temperature profile in the condenser. The lower temperatures near the condenser walls lead to contraction of the flow, and the flow streamlines deviate outward at the entrance of the condenser. Such bending of flow streamlines may lead to a shift in particle position at the condenser exit with respect to its position at the separator exit. However, the simulations indicate that for the intended operating conditions of the instrument, any such effects originating from temperature gradient are negligible.

Fig. 4 also shows simulated trajectories of uncharged particles. Since uncharged particles do not experience any electrostatic force in the separator, their trajectories remain close to the ground electrode. Due to large residence times these particles also experience large diffusional spreading. However, their transport is still confined to a narrow region near the ground electrode, ensuring that they do not interfere with the measurement of charged particles.

Fig. 4 also shows the contour profiles of grown droplet diameters in the condenser. The growth calculations were based on a particle with an initial diameter of 5 nm, following various particle trajectories in the condenser. The condensational growth is calculated using the flow, temperature, and saturation profiles obtained from FEM simulations described earlier. The calculations demonstrate that particles as small as 5 nm can be grown into optically detectable droplets ($> 120 \, \mu m$) using the proposed geometry and operating conditions.

4.4. Counting statistics of FIMS measurements

The improved time resolution of measurements often comes at the expense of reduction in counting statistics. The instrument design directly influences the counting statistics of size distribution measurements, and may limit the maximum frequency with which statistically significant measurements can be obtained. Counting statistics of FIMS measurements, using the proposed instrument geometry and flow conditions shown in Table 1, were investigated and are discussed below.

For each size bin, the uncertainty (σ_c) of particle counts measured by FIMS can be approximated, based on Poisson statistics, as $\sigma_c \approx \sqrt{C}$, where C is the number of particle counts detected in the corresponding size bin. C can be estimated as

$$C = Q_a t_c \eta \cdot \Delta N = Q_a t_c \eta \cdot \left(\frac{dN}{d \ln d_p} \right) \left(\frac{d \ln d_p}{d \ln Z_p} \right) \Delta \ln Z_p, \qquad (34)$$

where t_c is the sampling time, η is the particle bipolar charging probability, and N is the particle number concentration. The signal-to-noise ratio is given by $C/\sqrt{C} = \sqrt{C}$. Assuming that the counts detected by each unit of FIMS are grouped into 10 mobility size bins (evenly spaced on a logarithmic scale), and noting that each unit covers a factor of 10 in mobility, we have $\Delta \ln Z_p = (\ln 10)/10$. The counting statistics for measurement of typical remote continental and marine aerosol (Seinfeld & Pandis, 1998) were calculated using Eq. (34), and the results are shown in Fig. 5. FIMS provides substantial improvements in measurement counting statistics over traditional SMPS. For typical remote continental aerosols, 1 s measurement time is sufficient to obtain excellent counting statistics. For clean marine aerosols, measurement time of 8 s reasonably captures the main characteristics of the aerosol size distribution. The counting statistics of FIMS could be further improved by increasing the width b of the instrument channel and the aerosol flow rate.
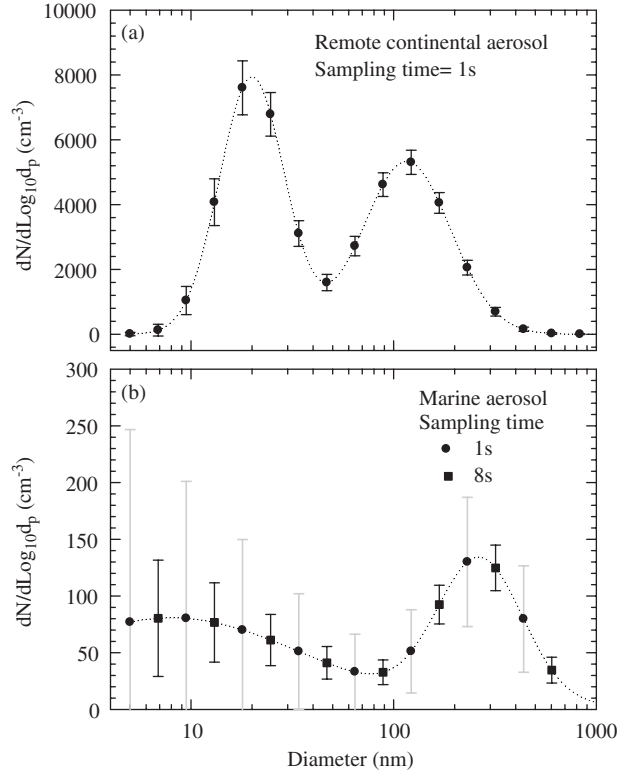
Fig. 5. Calculated counting statistics of FIMS measurements of (a) a typical remote continental aerosol for a sampling time of 1 s and (b) a typical marine aerosol for a sampling time of 1 and 8 s.

5. Effect of particle diffusion on FIMS transfer function

Knowledge of FIMS transfer function (or probability density function) that accounts for all measurement uncertainties is necessary in order to accurately derive aerosol size distributions from FIMS measurements. For non-diffusing particles, the uncertainty in measured mobility can be entirely attributed to finite stream width of aerosol flow. This uncertainty was discussed earlier, and the transfer function for a non-diffusing particle is given by Eq. (15). However, small particles with high diffusivity could further substantially increase the measurement uncertainties. Stolzenburg (1988) investigated the role of particle Brownian diffusion on the shape of DMA transfer function using an approach similar to that used by Tammet (1967) in his analysis of ion diffusion in aspiration condenser. More recently, Salm (2000) proposed a different approach to account for broadening of transfer function due to particle Brownian diffusion and/or turbulent diffusion. In this work we further extend the theoretical analysis developed earlier, which is similar to that of Stolzenburg (1988), to take into account the effect of particle Brownian diffusion on the FIMS transfer function $P(Z_p, \Psi_{out})$.

For a particle with mobility Z_p, the transfer function is given by

$$P(Z_p, \Psi_{out}) = \int_{\Psi_{1,in}}^{\Psi_{2,in}} f_e(\Psi_{in}) . f_{t-d}(Z_p, \Psi_{in}, \Psi_{out}) \, d\Psi_{in}, \tag{35}$$

where the definition of $f_e(\Psi_{in})$ remains same as in Eq. (7). $f_{t-d}(Z_p, \Psi_{in}, \Psi_{out})$ is modified to include particle Brownian diffusion, and is given by (Stolzenburg, 1988)

$$f_{t-d}(Z_p, \Psi_{in}, \Psi_{out}) = \frac{1}{\sqrt{2\pi}\sigma_\Gamma} \exp\left[-\frac{1}{2}\left(\frac{\Delta\Gamma}{\sigma_\Gamma}\right)^2\right], \tag{36}$$

where σ_Γ, known as spread factor, is the standard deviation of Γ. Calculation of spread factor will be discussed in detail later. From the definition of Γ given in Eq. (5), $\Delta\Gamma$ can be expressed as

$$\Delta\Gamma = \Gamma_{\text{out}} - \Gamma_{\text{in}} = \Psi_{\text{out}} - \Psi_{\text{in}} - Z_p\Delta\Phi. \tag{37}$$

Combining Eq. (35)–(37), the probability density function $P(Z_p, \Psi_{\text{out}})$ for a diffusing particle can be expressed as

$$P(Z_p, \Psi_{\text{out}}) = \frac{1}{\Psi_{2,\text{in}} - \Psi_{1,\text{in}}} \int_{\Psi_{1,\text{in}}}^{\Psi_{2,\text{in}}} \frac{1}{\sqrt{2\pi}\sigma_\Gamma} \exp\left[-\frac{1}{2}\left(\frac{\Psi_{\text{out}} - \Psi_{\text{in}} - Z_p\Delta\Phi}{\sigma_\Gamma}\right)^2\right] \mathrm{d}\Psi_{\text{in}}. \tag{38}$$

After performing the integration, Eq. (38) becomes

$$P(Z_p, \Psi_{\text{out}}) = \frac{1}{2}\frac{1}{\Psi_{2,\text{in}} - \Psi_{1,\text{in}}} \left\{\text{erf}\left(\frac{\Psi_{\text{out}} - \Psi_{1,\text{in}} - Z_p\Delta\Phi}{\sqrt{2}\sigma_\Gamma}\right) - \text{erf}\left(\frac{\Psi_{\text{out}} - \Psi_{2,\text{in}} - Z_p\Delta\Phi}{\sqrt{2}\sigma_\Gamma}\right)\right\}, \tag{39}$$

where the definition of error function has been used.

However, it is more convenient to express the probability density function $P(Z_p, \Psi_{\text{out}})$ as a function of response mobility Z_p^*, instead of Ψ_{out}. From the definition of Z_p^* given in Eq. (13), it can be seen that $P(Z_p, Z_p^*)=\Delta\Phi\, P(Z_p, \Psi_{\text{out}})$. Then,

$$\begin{aligned}
P(Z_p, Z_p^*) &= \frac{1}{2}\frac{\Delta\Phi}{\Psi_{2,\text{in}} - \Psi_{1,\text{in}}} \left\{\text{erf}\left(\frac{\Psi_{\text{out}} - \Psi_{1,\text{in}} - Z_p\Delta\Phi}{\sqrt{2}\sigma_\Gamma}\right) - \text{erf}\left(\frac{\Psi_{\text{out}} - \Psi_{2,\text{in}} - Z_p\Delta\Phi}{\sqrt{2}\sigma_\Gamma}\right)\right\} \\
&= \frac{1}{2}\frac{\Delta\Phi}{\Psi_{2,\text{in}} - \Psi_{1,\text{in}}} \left\{\text{erf}\left(\frac{(Z_p^* - Z_p)\Delta\Phi + \dfrac{\Psi_{2,\text{in}} - \Psi_{1,\text{in}}}{2}}{\sqrt{2}\sigma_\Gamma}\right) \right. \\
&\quad \left. - \text{erf}\left(\frac{(Z_p^* - Z_p)\Delta\Phi - \dfrac{\Psi_{2,\text{in}} - \Psi_{1,\text{in}}}{2}}{\sqrt{2}\sigma_\Gamma}\right)\right\}.
\end{aligned} \tag{40}$$

It can be shown by inserting Eq. (26) into Eq. (40) that

$$P(Z_p, Z_p^*) = \frac{1}{2\Delta Z_p^*}\left\{\text{erf}\left(\frac{(Z_p^* - Z_p + \frac{1}{2}\Delta Z_p^*)\Delta\Phi}{\sqrt{2}\sigma_\Gamma}\right) - \text{erf}\left(\frac{(Z_p^* - Z_p - \frac{1}{2}\Delta Z_p^*)\Delta\Phi}{\sqrt{2}\sigma_\Gamma}\right)\right\}. \tag{41}$$

The above equation is further non-dimensionalized using a normalized instrument response mobility $\tilde{Z}_p^*$, defined as $\tilde{Z}_p^* = Z_p^*/Z_p$. Then,

$$\begin{aligned}
P(Z_p, \tilde{Z}_p^*) &= P(Z_p, Z_p^*)\frac{\mathrm{d}Z_p^*}{\mathrm{d}\tilde{Z}_p^*} \\
&= \frac{1}{2\Delta Z_p^*}\left\{\text{erf}\left(\frac{(Z_p^* - Z_p + \frac{1}{2}\Delta Z_p^*)\Delta\Phi}{\sqrt{2}\sigma_\Gamma}\right) - \text{erf}\left(\frac{(Z_p^* - Z_p - \frac{1}{2}\Delta Z_p^*)\Delta\Phi}{\sqrt{2}\sigma_\Gamma}\right)\right\} Z_p \\
&= \frac{1}{2\Delta\tilde{Z}_p^*}\left\{\text{erf}\left(\frac{(\tilde{Z}_p^* - 1 + \frac{1}{2}\Delta\tilde{Z}_p^*)}{\sigma}\right) - \text{erf}\left(\frac{(\tilde{Z}_p^* - 1 - \frac{1}{2}\Delta\tilde{Z}_p^*)}{\sigma}\right)\right\},
\end{aligned} \tag{42}$$

where $\Delta\tilde{Z}_p^* = \Delta Z_p^*/Z_p$ and $\sigma = \sqrt{2}\sigma_\Gamma/Z_p\Delta\Phi$.

From the definition of $\tilde{Z}^*_{p_{\max}}$ introduced earlier in Eq. (30), expression for $P(Z_p, \tilde{Z}^*_p)$ can be further simplified to

$$P(Z_p, \tilde{Z}^*_p) = \frac{1}{2\beta\tilde{Z}^*_{p_{\max}}} \left\{ \mathrm{erf}\left(\frac{(\tilde{Z}^*_p - 1 + \frac{1}{2}\beta\tilde{Z}^*_{p_{\max}})}{\sigma}\right) - \mathrm{erf}\left(\frac{(\tilde{Z}^*_p - 1 - \frac{1}{2}\beta\tilde{Z}^*_{p_{\max}})}{\sigma}\right) \right\}, \tag{43}$$

Eq. (43) gives the probability density that a particle's mobility Z_p will be measured as normalized response mobility $\tilde{Z}^*_p$. $P(Z_p\tilde{Z}^*_p)$ reaches its maximum value at $\tilde{Z}^*_p = 1$ (i.e. when the response mobility Z^*_p is same as particle mobility Z_p). In the non-diffusing limit as $\sigma \to 0$, the first and second error function in Eq. (43) approach 1 and -1 respectively, and we have $P(Z_p, \tilde{Z}^*_p) \to 1/\beta\tilde{Z}^*_{p_{\max}}$.

Evaluation of $P(Z_p, \tilde{Z}^*_p)$ requires knowledge of non-dimensional spread factor σ that characterizes the broadening of the transfer function due to particle diffusion. An analytical expression for spread factor σ was obtained using analysis similar to that used by Stolzenburg (1988), and is presented in Appendix A. The expression of σ is given by

$$\sigma^2 = Pe^{-1}\left[2\left(\frac{a}{l_s}\right)^2 \tilde{x}^* + 72(1+\beta)^2 \tilde{Z}^2_{p_{\max}} \Theta(\tilde{x}^*)\right], \tag{44}$$

where Pe is the Peclet number defined as $Pe = Z_p E_x a/D = qV/k_B T$. Function $\Theta(\tilde{x}^*)$ is given by

$$\Theta(\tilde{x}^*) = \int_0^{\tilde{x}^*} \widetilde{x}^2(1-\widetilde{x})^2 \, d\widetilde{x} = \left(\frac{\tilde{x}^{*3}}{3} - \frac{\tilde{x}^{*4}}{2} + \frac{\tilde{x}^{*5}}{5}\right), \tag{45}$$

where $\tilde{x}^*$ is the location of centroid particle trajectory at the exit of the separator (normalized with respect to a). $\tilde{x}^*$ can be obtained by solving Eq. (22) for given Z^*_p, $Z^*_{p_{\max}}$, and β. The transfer function $P(Z_p, \tilde{Z}^*_p)$ can be calculated using Eqs. (43)–(45).

Fig. 6(a)–(c) show calculated transfer function $P(Z_p, \tilde{Z}^*_p)$ for particles of different sizes in Units 2, 3, and 4. Also shown are the values of $\tilde{Z}^*_{p_{\max}}$ corresponding to each particle size in respective unit. The shape of the transfer function varies considerably across different particle sizes and FIMS units. Since the transfer function is based on the normalized instrument response mobility, the width of the distribution is a direct measure of the relative uncertainty in measured mobility; wider the distribution, larger the relative uncertainty. For a given FIMS unit, the transfer function becomes narrower for particles with smaller diameters, indicating lower relative uncertainties in measured mobility. This may seem counterintuitive at first, considering the fact that smaller particles have larger diffusivities. However, it can be explained as follows. According to Eq. (43) width of the transfer function depends on two parameters $\beta\tilde{Z}^*_{p_{\max}}$ and σ. $\beta\tilde{Z}^*_{p_{\max}}$ accounts for uncertainties due to finite stream width of aerosol flow, whereas σ takes into account the spreading of transfer function due to Brownian diffusion. According to Eq. (43), width of the transfer function decreases with decreasing $\beta\tilde{Z}^*_{p_{\max}}$ and σ. Though the absolute uncertainty $\beta Z^*_{p_{\max}}$ remains constant regardless of the particle size (according to Eq. (27)), the relative uncertainty $\beta\tilde{Z}^*_{p_{\max}}$, however, decreases with increasing particle mobility (or decreasing particle size). Similarly, non-dimensional spread factor σ also decreases with increasing particle mobility, even though the dimensional spread factor (σ_Γ) increases with decreasing particle size. Increase in σ_Γ is only minor compared to the increase in particle mobility Z_p such that the net effect is decreasing σ with increasing Z_p. Thus, lower values of $\beta\tilde{Z}^*_{p_{\max}}$ and σ for small particles result in narrower transfer functions.

Fig. 6 also shows the transfer functions of 15, 48, and 173 nm particles measured in Units 2, 3, and 4, respectively. These particles correspond to the smallest sizes (highest mobilities) measured in their respective units ($\tilde{Z}^*_{p_{\max}} = 1$), and have similar centroid particle trajectory. As shown in Fig. 6, the FIMS transfer function becomes broader as the particle size decreases from 173 nm in Unit 4 to 15 nm in Unit 2. The spread factors (σ) for 15, 48, and 173 nm particles are 0.028, 0.009, and 0.003, respectively. For 15 nm particles in Unit 2, the transfer function exhibits substantial broadening due to Brownian diffusion. As Brownian diffusion becomes negligible for larger particles, the shape of the transfer function resembles a box function as shown earlier for a case of non-diffusing particles (Fig. 2(b)–(c)).
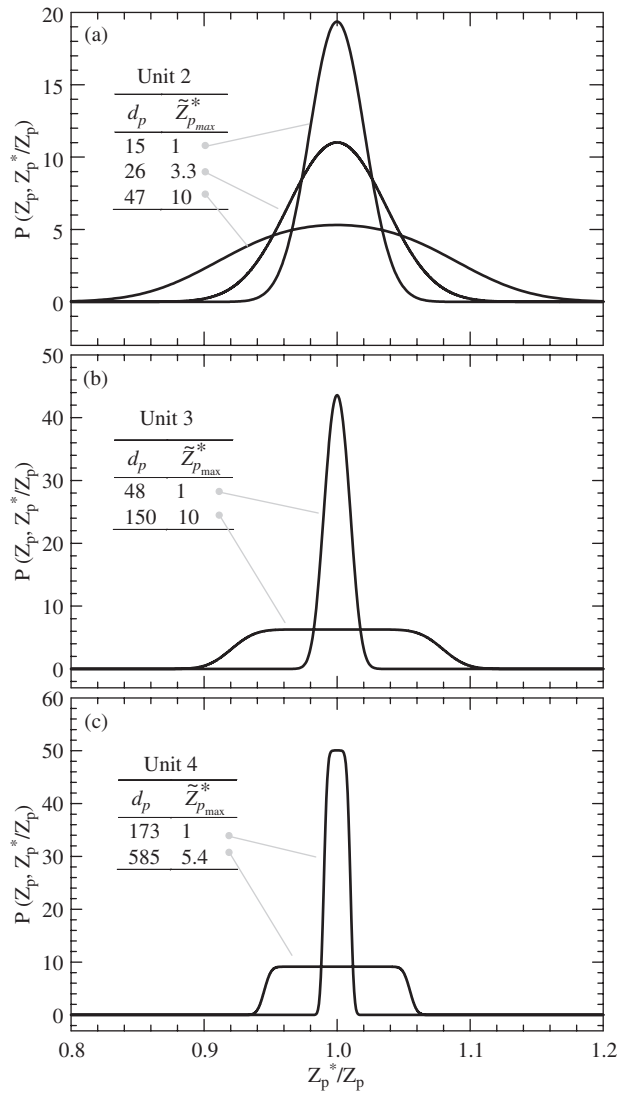
Fig. 6. Transfer functions of representative particle diameters in Units 2, 3, and 4.

6. Comparison of FIMS and DMA

6.1. Comparison of transfer functions of FIMS and DMA

Fig. 7 shows comparison of transfer functions of TSI cylindrical DMA and the FIMS for non-diffusing particles. The non-diffusing DMA transfer function was calculated for aerosol and sheath flow of 1 and 10 lpm respectively, and equal aerosol and monodisperse flows. Transfer function of FIMS is based on a total flow rate of $Q_t = 9.7$ lpm for a 1 μm particle, with other parameters listed in Table 1. The shapes of the transfer function are quite different for the two instruments. The DMA transfer function for non-diffusing particles is a triangle, whereas that of the FIMS is a rectangle. Also, shown in the inset in Fig. 7 are idealized transfer functions for both instruments. The base width of the non-diffusing DMA transfer function is $2\beta_{\mathrm{DMA}}$, with a height of unity. The width of the non-diffusing FIMS transfer function is $\beta \tilde{Z}^*_{p_{max}}$ with height equal to $1/(\beta \tilde{Z}^*_{p_{max}})$. For non-diffusing particles, the DMA transfer function remains same for particles with different mobilities. In contrast however, the FIMS transfer function becomes narrower as $\tilde{Z}_{p_{max}}$ decreases as discussed earlier (Fig. 6).
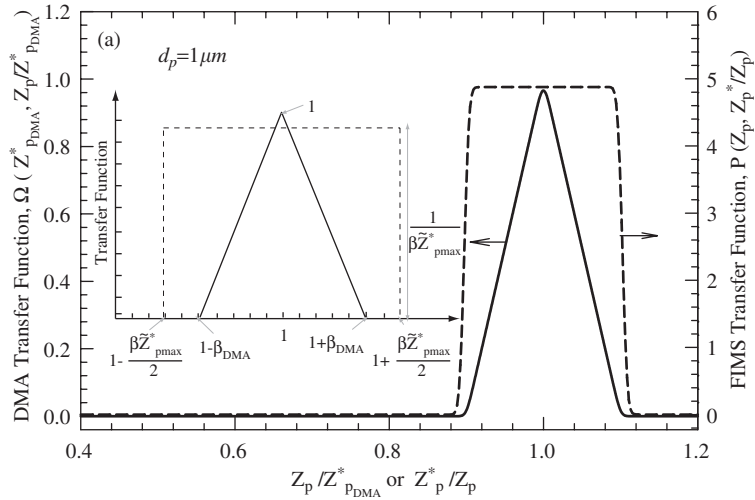
Fig. 7. Comparison of non-diffusing transfer functions of the TSI cylindrical DMA and the FIMS.
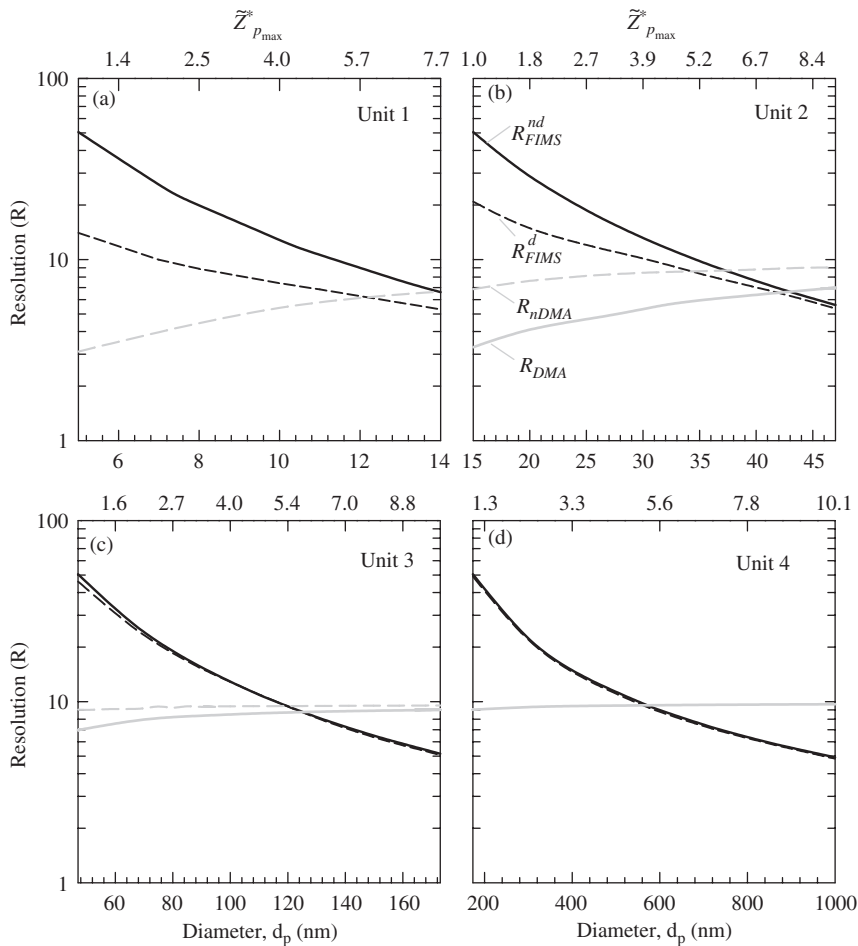

Fig. 8. Mobility resolution of the FIMS over the particle size range of 5–1000 nm. Also shown are the resolutions of TSI cylindrical DMA and nano-DMA.

Table 4
Mobility resolution of the particles measured by FIMS in Unit 2

d_p (nm) $\rightarrow$	Resolution			
	15 (1)[a]	26 (2.9)	36 (5.5)	47 (9.1)
Flow Q_t (lpm)				
7	17.8	10.2	7.5	5.2
9	19.7	11.3	7.8	5.4
11	21.5	12.3	8.3	5.5
13	23.6	13.0	8.5	5.5
15	25.2	13.4	8.7	5.5

A constant $Z^*_{p_{max}}$ of 9.75×10^{-7} m^2 V^{-1} s^{-1} and $\beta = 0.02$ were maintained at all flow rates.

[a]Numbers in parenthesis indicate $\tilde{Z}^*_{p_{max}}$ for each diameter.

6.2. Comparison of mobility resolution of FIMS and DMA

When particle Brownian diffusion is taken into account, the FIMS mobility resolution $R^d_{FIMS} \left(\frac{Z_p}{\Delta Z^*_{fwhh}} \right)$ can be calculated using Eq. (43). Fig. 8(a)–(d) show the resolution R^d_{FIMS} of all four FIMS units over the size range of 5 nm–1 μm. Also plotted in each figure is mobility resolution of non-diffusing particles (R^{nd}_{FIMS}) based on Eq. (30). For comparison, Fig. 8 also presents the mobility resolutions of TSI cylindrical DMA (R_{DMA}) and TSI nano-DMA (R_{nDMA}), that take into account particle diffusion. Resolutions of the two DMA were calculated using an aerosol flow rate of 1 lpm, and sheath flow rate of 10 lpm.

The resolution of FIMS for non-diffusing particles (R^{nd}_{FIMS}) decreases with increasing diameter in each unit from about 50 at $\tilde{Z}^*_{p_{max}} = 1$ to about 5 at $\tilde{Z}^*_{p_{max}} = 10$ in each unit. This is characteristically different, and apparently counterintuitive, in comparison to the trend in the DMA resolution. For both cylindrical and nano DMAs, the resolution of non-diffusing particles is constant, and is given by the reciprocal of aerosol-to-sheath flow rate ratio ($1/\beta_{DMA}$). Irrespective of particle size, all (non-diffusing) particles have the same centroid particle streamline in DMA. Consequently, at a given aerosol and sheath flow rate, resolution of DMA remains constant. However in case of FIMS, since each particle follows a different trajectory, the ratio of aerosol flow to the total flow bounded by the particle trajectory at the separator exit is different. This can be further explained by transforming Eq. (30) using a position-dependent ratio of flow rates β_x, defined as $\beta_x = Q_a/Q(\tilde{x}^*)$. Then, resolution R of FIMS for a non-diffusing particle can be written as

$$R = \frac{Z_p}{\Delta Z^*_p} = \frac{Q(\tilde{x}^*) - (Q_a/2)}{Q_a} = \frac{1 - \frac{1}{2}\beta_x}{\beta_x} \cong \frac{1}{\beta_x}. \tag{46}$$

Thus analogous to the case of DMA, Eq. (46) shows that the mobility resolution of FIMS for non-diffusing particles is given by the reciprocal of specific flow rate ratio β_x. Since β_x decreases with increasing $\tilde{x}^*$, the resolution increases with increasing particle mobility. Note that, for particle with maximum mobility ($Z^*_{p_{max}}$) measured by FIMS, $Q(\tilde{x}^*) = Q_t$, $\beta_x = \beta$, and the resolution of the FIMS reaches its maximum value of $1/\beta$.

Comparison of R^d_{FIMS} and R^{nd}_{FIMS} in Units 1 and 2 clearly shows the degradation of FIMS resolution due to particle diffusion. As particle diffusivity becomes negligible in Units 3 and 4, the resolution based on Eq. (43) is very close to that given by Eq. (30). Mobility resolution of FIMS (R^d_{FIMS}) is higher than that of nano-DMA for particles smaller than ~ 12 nm($\tilde{Z}^*_{p_{max}} = 5.7$) in Unit 1 and ~ 35 nm($Z_{p_{max}} = 5.21$) in Unit 2. R^d_{FIMS} falls below that of DMA in Units 3 and 4 at $\tilde{Z}^*_{p_{max}}$ greater than about 5. As discussed earlier in the design considerations, the operating conditions of FIMS are chosen assuming a minimum acceptable mobility resolution of 5. The mobility resolution of FIMS can be further improved by reducing the flow rate ratio β as shown in later discussions.

The influence of total flow rate Q_t and flow rate ratio β on the resolution of FIMS was also investigated. Table 4 shows mobility resolution of FIMS (R^d_{FIMS}) at various total flow rates for a range of particle diameters. The voltage across the electrodes in the separator was changed accordingly to maintain the same measurement range for each case. Particles with $\tilde{Z}^*_{p_{max}}$ closer to unity (smaller particles) exhibit greater improvement in resolution with increasing Q_t.

Table 5
Mobility resolution of FIMS in Unit 2 at different β values

β	Resolution				
	d_p	15 nm	26 nm	36 nm	47 nm
	$\tilde{Z}_{p_{max}}^*$	1	2.9	5.5	9.1
0.050		16.2	6.8	3.7	2.2
0.033		18.8	9.4	5.4	3.3
0.025		20.0	10.7	6.9	4.4
0.020		20.9	11.6	8.0	5.4
0.017		20.7	12.1	8.7	6.2
0.014		20.9	12.5	9.3	7.0

A constant $Z_{p_{max}}^*$ of $9.75 \times 10^{-7} \, \text{m}^2 \, \text{V}^{-1} \, \text{s}^{-1}$ and $Q_t = 9.7$ lpm were maintained at all flow rates.

Table 6
Mobility resolution of FIMS in Unit 2 with different separator lengths (l_s)

l_s (cm)	Resolution				
	d_p	15 nm	26 nm	36 nm	47 nm
	$\tilde{Z}_{p_{max}}^*$	1	2.9	5.5	9.1
5		36.7	16.5	9.2	5.6
10		28.2	14.3	9.0	5.6
15		23.6	13.0	8.5	5.5
20		20.9	11.6	8.0	5.4

A constant $Z_{p_{max}}^*$ of $9.75 \times 10^{-7} \, \text{m}^2 \, \text{V}^{-1} \, \text{s}^{-1}$ and $Q_t = 9.7$ lpm were maintained at all flow rates.

The resolution of 15 and 26 nm particles increased by 40% and 30% respectively, when the total flow rate is increased from 7 to 15 lpm. In contrast, resolution of 47 nm particles increases only by 1.7%. Increasing Q_t reduces the particle residence time in the separator, which leads to smaller diffusional spreading of particles. Since the broadening of transfer function due to particle diffusion is substantial for smaller particles with high diffusivity, increasing Q_t will result in greater improvements in mobility resolution for small particles. For larger particles however, the uncertainty in measured mobility is mainly dictated by flow rate ratio β. As a result, increasing Q_t does not have a significant effect on mobility resolution of larger particles. Table 5 shows FIMS resolution at various aerosol-to-sheath flow rate ratios (β). β has a strong influence on the measurement resolution, especially for large particles. Resolution increases by 29% for 15 nm particle, 83% for 26 nm, 150% for 36 nm, and 218% for 47 nm particle as β is reduced from 0.05 to 0.014. This clearly indicates that the mobility resolution of larger particles can be significantly improved by operating the instrument at lower β.

While the degradation of resolution due to particle diffusion can be reduced by increasing the total flow rate Q_t, a higher total flow requires longer condenser to grow particles into detectable droplets, which may further lead to much longer condenser length. An alternative approach would be to reduce the length of the separator, similar to the design of the nano-DMA that increases the mobility resolution by reducing its column length. Table 6 shows the mobility resolution for particles measured by Unit 2 with different separator lengths. Again, same measurement range was maintained for all cases by varying the separator voltage. As expected, reducing the separator length results in greater improvement in the resolution of smaller particles. Resolution of 15 nm particles increases from 20.9 to 36.7 whereas the resolution of 47 nm particles only increases from 5.4 to 5.6.

The best mobility resolution can be achieved in each unit by using the shortest possible separator length. However, in the suggested FIMS configurations in Table 1 for Units 2–4, separator length was maintained constant for all units. Advantage of such a design is that a single unit can be interchangeably used as Units 2–4 by simply changing the separator voltage.

7. Summary and conclusions

A novel Fast Integrated Mobility Spectrometer (FIMS) is described for characterizing aerosol size distributions with high-time and size resolution, and excellent counting statistics. FIMS combines electrical mobility-based classification and particle counting in a single unit, and eliminates the need for voltage scanning required in traditional scanning Differential Mobility Analyzer (DMA) techniques. As a result, aerosol size distributions can be obtained at sub-second time intervals.

A theoretical framework has been developed to obtain the transfer function of a single FIMS, unit accounting for uncertainties originating from particle Brownian diffusion, and finite stream width of aerosol flow. The FIMS transfer function was used to characterize measurement resolution of the instrument over a wide range of operating conditions. Results show that a decade of mobility can be measured in a single FIMS unit with a minimum mobility resolution of 5. The mobility resolution of a single FIMS unit increases with decreasing particle size, which is attributed to the higher specific flow rate ratios for smaller particles. Compared to conventional cylindrical DMA operated under typical operating conditions, the resolution of FIMS is much higher for smaller particles, and is comparable to that of DMA for larger particles. The counting statistics of FIMS measurements were also investigated. It was shown that for a typical remote continental aerosol, 1 s measurement time provides excellent signal-to-noise ratio.

Detailed numerical simulations were also carried out to study the particle transport and growth kinetics in FIMS. Results indicate excellent activation efficiencies for particles larger than 5 nm. Particles as small as 5 nm can be grown into droplets larger than 120 μm to facilitate their reliable optical detection.

Appendix A

This appendix describes the derivation of spread factor σ required to evaluate $P(Z_p, \tilde{Z}_p^*)$ in Eq. (43). Similar to the work of Stolzenburg (1988), a few approximations were made in the derivation of the spread factor. It was assumed that only diffusion in the direction orthogonal to the particle stream function (cross-stream direction denoted by χ; see Fig. 2) was significant, and streamwise (s-direction) diffusion was negligible. Particle losses to the walls of the separator were also neglected. The root-mean-square displacement of particles from the centroid particle trajectory is a function of time according to Einstein equation (Fuchs, 1964)

$$d\langle \chi^2 \rangle = 2D \, dt. \tag{47}$$

The distribution of particles is Gaussian with variance $\sigma_\chi^2 = \langle \chi^2 \rangle$. σ_χ can be related to σ_r by (Stolzenburg, 1988)

$$\sigma_\Gamma = \left(\frac{\partial \Gamma}{\partial \chi} \right) \sigma_\chi. \tag{48}$$

With $\chi = 0$ on the particle stream line Γ, the variation of Γ with χ can be approximated by the Taylor series expansion (Stolzenburg, 1988):

$$\Gamma(\chi, s) \cong \Gamma|_{\chi=0} + \left. \frac{\partial \Gamma}{\partial \chi} \right|_{\chi=0}. \tag{49}$$

Let **r** represent the particle position vector, at $\chi = 0$, both $\partial\mathbf{r}/\partial\chi$ and $\nabla\Gamma$ are perpendicular to the particle streamline and we have

$$\frac{\partial\Gamma}{\partial\chi} \cong \left|\frac{\partial\mathbf{r}}{\partial\chi}\right|.|\nabla\Gamma| = (1).\sqrt{v_x^2 + v_y^2} = v, \tag{50}$$

where v is the magnitude of particle velocity. Combining Eqs. (48) and (50), we have

$$\sigma_\Gamma = v\sigma_\chi. \tag{51}$$

Since the particle diffusivity D is constant, total diffusional spreading can then be calculated by integrating σ_Γ over the path of the trajectory (Stolzenburg, 1988):

$$\sigma_\Gamma^2 = \int_{\text{entrance}}^{\text{exit}} d\sigma_\Gamma^2 = \int_{\text{entrance}}^{\text{exit}} d(v\sigma_\chi^2) = \int_{\text{entrance}}^{\text{exit}} v^2\,d(\sigma_\chi^2) = 2D\int_{\text{entrance}}^{\text{exit}} v^2\,dt. \tag{52}$$

The particle velocity is given by

$$v^2 = v_x^2 + v_y^2 = u_y^2(\tilde{x}) + (Z_p E_x)^2, \tag{53}$$

where $u_y(\tilde{x})$ can be evaluated using Eq. (20). Inserting Eq. (53) into Eq. (52), we have

$$\sigma_\Gamma^2 = 2D\int_{\text{entrance}}^{\text{exit}} \left[\left(\frac{6Q_t}{ab}[\tilde{x}(1-\tilde{x})]\right)^2 + (Z_p E_x)^2\right] dt. \tag{54}$$

Noting $\tilde{x} = (v_x t)/a = (Z_p E_x t)/a$, we can change the integration variable t in Eq. (54) to $\tilde{x}$:

$$\sigma^2 = \frac{2\sigma_\Gamma^2}{(Z_p\Delta\Phi)^2} = \frac{4D}{(Z_p\Delta\Phi)^2} \int_0^{\tilde{x}^*} \left[\left(\frac{6Q_t}{ab}[\tilde{x}(1-\tilde{x})]\right)^2 + (Z_p E_x)^2\right]\left(\frac{a}{Z_p E_x}\right) d\tilde{x}, \tag{55}$$

where x^* is the location of the particle centroid trajectory at the separator exit. After carrying out the integration, we can simplify the above equation to

$$\sigma^2 = Pe^{-1}\left[2\left(\frac{a}{l_s}\right)^2 \tilde{x}^* + 72(1+\beta)^2 \tilde{Z}_{p\max}^2 \Theta(\tilde{x}^*)\right], \tag{56}$$

where Pe is the Peclet number defined as $Pe = Z_p E_y a/D = qV/k_B T$, q is the total electric charge on the aerosol particle, k_B is Boltzmann's constant, and T is the temperature. Function $\Theta(\tilde{x}^*)$ is given by

$$\Theta(\tilde{x}^*) = \int_0^{\tilde{x}^*} \tilde{x}^2(1-\tilde{x})^2\,d\tilde{x} = \left(\frac{\tilde{x}^{*3}}{3} - \frac{\tilde{x}^{*4}}{2} + \frac{\tilde{x}^{*5}}{5}\right), \tag{57}$$

where $\tilde{x}^*$ can be obtained by solving Eq. (22) for given Z_p^*, $Z_{p\max}^*$, and β.

References

Bird, R. B., Stewart, W. E., & Lightfoot, E. N. (1960). *Transport phenomena*. New York: Wiley.

Brock, C. A., Schröder, F., Kärcher, B., Petzold, A., Rusen, R., & Fiegbig, M. (2000). Ultrafine particle size distributions measured in aircraft exhaust plumes. *Journal of Geophysical Research*, *105*, 26,555–26,567.

Ermak, D. L. (1975). Computer simulation of charged particles in solution. I: technique and equilibrium properties. *Journal of Chemical Physics*, *62*, 4189–4196.

Flagan, R. C. (1998). History of electrical aerosol measurements. *Aerosol Science and Technology*, *28*(4), 301–380.

Flagan, R. C. (1999). On differential mobility analyzer resolution. *Aerosol Science and Technology*, *30*(6), 556–570.

Fuchs, N. A. (1964). *The mechanics of aerosols*. Oxford: Pergamon Press.

Hering, S. V., & McMurry, P. H. (1991). Optical counter response to monodisperse atmospheric aerosols. *Atmospheric Environment Part A*, *25*(2), 463–468.

Johnson, T., Caldow, R., Pocher, A., Mirme, A., & Kittelson, D. (2004). A new electrical mobility particle sizer spectrometer for engine exhaust particle measurements. *SAE 2004 World congress & exhibition* SAE-2004-01-134, Detroit, MI.

Knutson, E. O., & Whitby, K. T. (1975). Aerosol classification by electric mobility: Apparatus, theory, and applications. *Journal of Aerosol Science*, *6*, 443–451.

Mirme, A. (1994). *Electrical aerosol spectrometry*. Ph.D. Thesis, Universitatis Tartuensis, Tartu, Estonia.

Mirme, A., Noppel, M., Peil, I., Salm, J., Tamm, E., Tammet, H., 1984. Multi-channel electric aerosol spectrometer. In *11th international conference on atmospheric aerosols, condensation and ice nuclei*, Budapest (Vol. 2, pp. 155–159).

Russell, L. M., Flagan, R. C., & Seinfeld, J. H. (1995). Asymmetric instrument response resulting from mixing effects in accelerated DMA-CPC measurements. *Aerosol Science and Technology*, *23*, 491–509.

Salm, J. (2000). Diffusion distortions in a differential mobility analyzer: The shape of apparent mobility spectrum. *Aerosol Science and Technology*, *32*(6), 602–612.

Seinfeld, J. H., & Pandis, S. N. (1998). *Atmospheric chemistry and physics*. New York: Wiley.

Stolzenburg, M. (1988). *An ultrafine aerosol size distribution measuring system*. Ph.D. thesis, St. Paul, University of Minnesota.

Tammet, H. (1967). *Aspiration method for the determination of atmospheric ion spectra*, (Vol II). Jerusalem: Israel program for scientific translations.

Tammet, H., Mirme, A., & Tamm, E. (1998). Electrical aerosol spectrometer of Tartu University. *Journal of Aerosol Science*, *29*, S427–S428.

Tammet, H., Mirme, A., & Tamm, E. (2002). Electrical aerosol spectrometer of Tartu University. *Atmospheric Research*, *62*, 315–324.

Wang, S. C., & Flagan, R. C. (1989). Scanning electrical mobility spectrometer. *Journal of Aerosol Science*, *20*, 1485–1488.

Wang, J., McNeill, V. F., Collins, D. R., & Flagan, R. C. (2002). Fast mixing condensation nucleus counter: Application to rapid scanning differential mobility analyzer measurements. *Aerosol Science and Technology*, *36*(6), 678–689.